Tensile and Fracture Characterization of PETI-5 and IM7/PETI-5 Graphite/Epoxy Composites Under Quasi-Static and Dynamic Loading Conditions

Dongyeon Lee
Post-Doctoral Fellow

Hareesh V. Tippur[1]
McWane Professor
ASME Fellow
e-mail: tippuhv@auburn.edu

Department of Mechanical Engineering,
Auburn University,
Auburn, AL 36830

Brian J. Jensen

Philip B. Bogert

NASA Langley Research Center,
Hampton, VA 44313

Tensile and fracture responses of the phenylethynyl terminated imide oligomer (PETI-5) are studied. Since this polymer is a candidate aerospace structural adhesive as well as a matrix material in composite systems, neat as well as fiber reinforced forms of PETI-5 are studied under static and dynamic loading conditions. A split-Hopkinson tension bar apparatus is used for performing tensile tests on dogbone specimens. The dynamic fracture tests are carried out using a drop tower in conjunction with 2D image correlation method and high-speed digital photography on edge cracked specimens in three-point bend configuration. A toughened neat epoxy system, Hexcel 3900, is also studied to provide a baseline comparison for neat PETI-5 system. The tensile stress-strain responses show PETI-5 to have excellent mechanical characteristics under quasi-static and dynamic loading conditions when compared with 3900. Fracture behavior of PETI-5 under quasi-static and impact loading conditions also shows superiority relative to 3900. The dynamic fracture behavior of a PETI-5 based graphite fiber reinforced composite, IM7/PETI-5, is also studied and the results are comparatively evaluated relative to the ones corresponding to a more common aerospace composite system, T800/3900-2 graphite/epoxy. Once again, the IM7/PETI-5 system shows excellent fracture performance in terms of dynamic crack initiation and growth behaviors. [DOI: 10.1115/1.4003487]

Keywords: adhesives, graphite/epoxy composites, fracture, tensile behavior, strain rate effects, digital image correlation, split-Hopkinson bar

1 Introduction

The high-speed research (HSR) program was launched in the early 1990s by NASA's Office of Aeronautics along with a team of U.S. aerospace companies in order to develop technology for a Mach-2.4 high-speed civil transport (HSCT) passenger jet [1]. The technological focus was not only on propulsion and aerodynamic performance but also on structural materials used for airframe construction. At supersonic speeds, the aircraft is expected to experience severe thermomechanical loads for extended periods of time. For research purposes, high safety margins are to be set so that the candidate materials withstand 177°C for 60,000 h, equivalent to lifetime service hours. During this period of time, the structural materials are to perform well in many aspects including toxicity of by-products, susceptibility to moisture and solvents, microcracking under hygrothermal fatigue, as well as mechanical performance over a wide range of temperatures. After considering numerous candidate materials, NASA Langley Research Center developed a promising material, designated LaRC phenylethynyl terminated imide oligomers fifth composition (PETI-5) to be used as an adhesive as well as a matrix material in composites. This material has a unique combination of properties including superior mechanical properties and thermal stability, excellent resistance to aircraft fluids, and easy processing in an autoclave. To date, a composite system, PETI-5 reinforced with IM7 graphite fiber, has displayed promising performance, meeting the requirements of the HSCT program [2–7].

During a supersonic flight, aerodynamic loading causes transient heating and hence studies on IM7/PETI-5 composites reported in literature up to now have mainly focused on thermal properties. This, in turn, affects mechanical performance as well and is yet to be fully addressed. Since most of the outer body of the HSCT would be fabricated from graphite fiber reinforced composites, it is necessary to investigate and understand the response of the material at elevated rates of loading. Accordingly, in this work, quasi-static and dynamic tensile and fracture performances of neat PETI-5 are studied using various testing techniques: strain gauge method, ultrasonic measurements, tensile split-Hopkinson bar apparatus, 2D digital speckle correlation method, and high-speed photography. The mechanical performance of PETI-5 is also evaluated relative to another epoxy resin system used by the aerospace industry, Hexcel 3900. Finally, dynamic mode-I and mixed-mode fracture responses of unidirectional IM7/PETI-5 composites are presented for two different fiber orientations. Again, the fracture response results are examined relative to an alternative graphite/epoxy composite, T800/3900-2, studied under similar loading conditions.

In what follows, a brief description of PETI-5 and its composite are provided. This is followed by tensile failure responses of neat PETI-5 under quasi-static and dynamic loading conditions including a brief description of tensile split-Hopkinson bar apparatus used for studying the latter. Subsequently, a brief description of digital image correlation (DIC) and the experimental apparatus used for studying quasi-static and dynamic fracture behaviors in neat and composite coupons is provided before presenting PETI-5

[1]Corresponding author.

Contributed by the Materials Division of ASME for publication in the JOURNAL OF ENGINEERING MATERIALS AND TECHNOLOGY. Manuscript received August 30, 2010; final manuscript received December 15, 2010; published online March 21, 2011. Assoc. Editor: Thomas Siegmund.

results relative to the ones for 3900. The dynamic fracture responses and parameters of PETI-5 based graphite fiber reinforced composites are compared with the ones made of 3900 using both direct optical measurement and fracture surface morphology before summarizing the results of this work.

2 Compositional Details of PETI-5 and PETI-5 Composite

In an effort to produce an adhesive and composite matrix with the combination of properties required to meet the performance goals of a HSCT, many different PETIs were synthesized at various molecular weights [8]. Five of these compositions were scaled-up and characterized as both an adhesive and a composite. The fifth one was selected for the program. PETI-5 was prepared at a calculated molecular weight of 5000 g/mol by reacting biphenyldianhydride (BPDA) with 3,4′-oxydianiline (85%) and 1,3-(3′-aminophenoxy benzene) (15%) and endcapping with phenylethynyl phthalic anhydride (PEPA) in N-methylpyrrolidinone (NMP) at 35% solids by weight. Chain length of the base oligomer controls the crosslink density and thus material characteristics such as glass transition temperature, viscosity, modulus, strength, and toughness. Therefore, low molecular weight results in low melt viscosity, high modulus and strength, and low toughness. Selecting the right molecular weight provides the best combination of properties for the requirements of a given application. For the current work, along with mechanical and thermal properties, good toughness was needed to translate into composite open-hole compression strength and compression after impact strength as well as sufficiently low viscosity for the autoclave process. A molecular weight of 5000 g/mol was chosen so that viscosity is low enough for the process yet high enough to give high toughness.

The prepared polyamide acid/NMP solution was used to prepare unidirectional prepreg by solution coating of the IM7 graphite fiber. To produce a material with tack and drape, ~20% NMP by weight was allowed to remain in the prepreg. Composites were fabricated in an autoclave using a vacuum bag and consolidation pressure of 1.38×10^6 Pa with a final cure temperature of 371°C for 1 h. At this cure temperature and molecular weight, PETI-5 reacts to form a lightly cross-linked polyimide network. To prepare PETI-5 powder for neat resin moldings, toluene was added to the PETI-5 amide acid solution, heated to reflux (~110°C) overnight, and finally to ~160°C by collecting the toluene/water azeotropic mixture. The imidized PETI-5 oligomers precipitated from solution and the resulting mixture was washed in water, then methanol followed by drying at 150°C. The powders were compression molded under 0.69×10^6 Pa at 371°C for 1 h to produce void free, high quality moldings.

3 Tensile Tests on Neat PETI-5

Several static tests on neat PETI-5 were first carried out to ensure that the properties of as-received material were comparable to the ones reported in literature. Dogbone specimens were tested in a universal testing machine in displacement control mode (cross-head speed 0.005 mm/s). A combination of a strain gauge, an extensometer, and an optical grid pattern were used to measure Young's modulus (E), Poisson's ratio (ν), stress-strain history, ultimate stress, and failure strain. The results are summarized in Table 1 along with the ones reported for PETI-5 in literature. Evidently the in-house measurements are in good agreement with those published in literature.

Dynamic elastic constants were evaluated from wave speed measurements in cast PETI-5 sheets using ultrasonic pulse-echo transducers, as described in Ref. [10]. Average longitudinal wave speed (c_l) was found to be 2525 ± 15 m/s and shear wave speed (c_s) was found to be 1095 ± 5 m/s. With the material density (1335 ± 25 kg/m^3) known, dynamic Young's modulus and Poisson's ratio were found to be 4.46 GPa and 0.384, respectively.

Table 1 Quasi-static tensile properties of PETI-5 (as-received at room temperature)

	E (GPa)	ν	σ^u (MPa)	ε^u (%)
Ref. [9]	2.81	-	116.5	32
LaRC	3.14	-	129.6	35
Current	3.25 (±0.2)	0.37 (±0.01)	116.4 (±2.4)	32.8 (±1.2)

When compared with the quasi-static values, dynamic Young's modulus is about 37% higher, whereas Poisson's ratio shows negligible loading rate sensitivity.

The dynamic tensile tests were carried out using a tensile split-Hopkinson pressure bar (SHPB) apparatus for evaluating high-strain rate behavior of PETI-5. In order to subject the specimens to tensile stress pulses, an especially designed gripping method [11] was used (see Fig. 1). An optimally shaped dogbone specimen was held between the incident and transmission bars, both made of 12.5 mm diameter Al 7075-T6 rods, using matching slots machined at the ends of the two bars. A hollow striker, also made of aluminum, (inner diameter: 12.5 mm, outer diameter: 25.4 mm, and length: 381 mm) riding over the incident bar was propelled by compressed air to strike a stopper (anvil) at the impacting end of the incident bar. The compressed air pressure was used to control striker velocity and, in the current work, velocity at impact was set to ~14 m/s. The recorded strain signals from both the incident and transmitted bars were used to calculate instantaneous specimen stress (σ) and strain (ε) histories using standard SHPB equations

$$\sigma(t) = E_0\frac{A_0}{A}\varepsilon_T(t)$$

$$\dot{\varepsilon}(t) = -\frac{2c_0}{L}\varepsilon_R$$

$$\varepsilon(t) = -\frac{2c_0}{L}\int_0^t \varepsilon_R dt \tag{1}$$

where $\dot{\varepsilon}$ is the strain rate, A_0 and A indicate cross-sectional area of the two bars and specimen, respectively, c_0 is the wave speed in the bars, E_0 is the elastic modulus of the bars, and L is the gauge length of the specimen.

The resulting dynamic stress-strain responses (determined using only the incident and transmitted signals) for neat PETI-5 for a strain rate of $\dot{\varepsilon}\sim2000$ s^{-1} are shown in Fig. 2 (the raw voltage signals from strain gauges recorded during SHPB tests for PETI-5 are shown in the Appendix). Considering the transient nature of loading, good repeatability between the two data sets can be

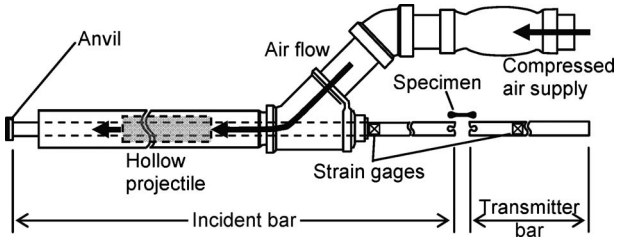

Fig. 1 Schematic of tensile SHPB apparatus used for testing dogbone specimens at high-strain rates

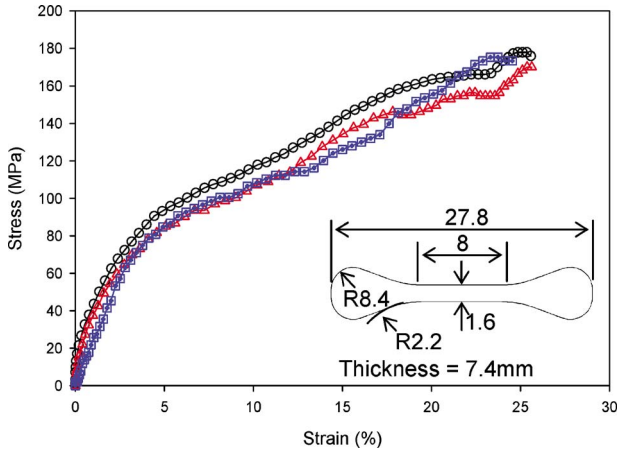

Fig. 2 Tensile stress-strain responses for four PETI-5 dynamic tensile tests carried out using split-Hopkinson bar apparatus (strain rate ~2000/s). Inset shows geometry of a dogbone specimen used in the test (units in mm).

readily seen. The dynamic ultimate strain was found to be ~30% lower than the one for the quasi-static case, 24.4% (±1.2) showing a tendency to embrittle modestly at higher strain rates.[2] The average dynamic ultimate strength measured from two specimens here is approximately 174.4 (±4.0) MPa, nearly 50% higher than the one measured quasi-statically ($\dot{\varepsilon} < 10^{-2}$ s^{-1}).

4 Fracture of Neat PETI-5

Fracture tests were carried out on samples in three-point symmetric bending configuration on edge cracked beams under quasi-static loading. In these tests, 2D DIC technique was used to monitor full-field in-plane deformations in the crack tip vicinity. To implement DIC, the surface of the specimen was sprayed with mists of black-and-white paint to create a random speckle pattern.

The basic idea of 2D DIC technique in the context of fracture mechanics is to track clusters of decorated speckles on a planar specimen surface during a fracture event to quantify in-plane displacements. The photographed gray scales recorded by a digital camera before and after deformation are correlated for extracting 2D planar displacement components. In this work, digitized light intensity data are analyzed using in-house image processing algorithms implemented in the MATLAB™ environment. A multistep approach similar to the one described in Refs. [12,13] was employed for measuring displacements at discrete locations of a rectangular grid in the field of view. (1) Displacements were coarsely estimated by performing 2D cross-correlation between images of the deformed and undeformed states in the Fourier domain. (2) The displacements from step (1) were refined using an iterative nonlinear least-squares minimization of a 2D correlation coefficient in the spatial domain. (3) Smoothing of crack tip displacements, if needed,[3] using an algorithm applied to (u,v) displacement fields separately. The smoothing method in the current work employed an unbiased optimum smoothing parameter based on the noise level present in the displacement field [14,15].

[2]The failure of specimen was assessed based on the SHPB signals and not based on direct optical evidence. Hence, the failure strain value reported is only an estimate.

[3]Although the second step yields accurate estimation of displacements, the resulting data could be noisy due to the choice of the subimage size, number of overlapping pixels of neighboring subimages, accuracy of the minimization scheme used, etc. Therefore, for a better interpretation of the resulting displacement fields and for obtaining strain components, if needed, additional smoothing step is desirable. However, the displacement data from either the second or third step yield negligible difference in fracture parameter estimates.

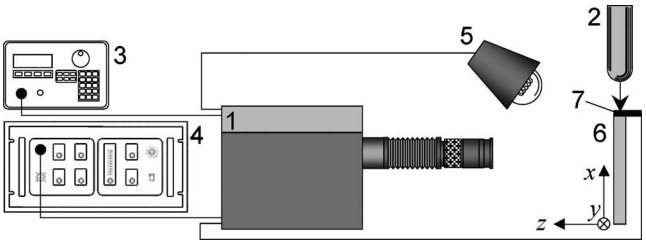

Fig. 3 Schematic of the experimental set-up for dynamic fracture: (1) high-speed digital camera, (2) impact tup of the drop tower, (3) delay generator, (4) lamp control unit, (5) pair of light sources, (6) specimen, and (7) copper tape

During quasi-static tests, three-point bend samples were loaded in a displacement controlled mode (cross-head speed =0.005 mm/s). The decorated speckle images were recorded at various instants of time (and hence load levels) using time-lapse digital photography until complete fracture. Each image (20 × 30 mm^2) was recorded as an eight-bit (0–255) gray scale with a pixel resolution of 1000 × 1500 using a Nikon D100 digital SLR camera. Each subimage size was 30 × 30 pixels, resulting in approximately 32 × 49 subimages per image. (This remained the same throughout this study in the case of static fracture tests.) The speckle patterns at each load level were then correlated with the one recorded under no-load condition. As described previously, correlation of an image before loading with the one at a given load level produces displacement fields. After refining these fields, the stress intensity factors were computed by using measured displacement components in conjunction with plane stress crack tip displacement fields (to be discussed subsequently). An overdeterministic least-squares analysis method was adopted to estimate the stress intensity factors. The resulting stress intensity factor histories will be discussed in Sec. 5 along with the ones for Hexcel 3900.

Dynamic fracture response was also measured for neat PETI-5 beam specimens by subjecting them to one-point impact (edge cracked specimens were supported on two soft putty blocks and subjected to impact loading) in symmetric mode-I loading configuration. Edge cracked PETI-5 beams of size and geometry identical to those tested in quasi-static experiments were used. The evolution of dynamic fracture parameters during impact loading was determined using 2D digital image correlation method and high-speed photography (framing rate 200,000–250,000 frames/s) by measuring displacement fields in the crack tip vicinity. The schematic of the experimental set-up used in these tests is shown in Fig. 3.

It consisted of an Instron-Dynatup 9250-HV drop tower for delivering low-velocity impact (impact velocity ~4.8 m/s) and a Cordin-550 high-speed digital camera for capturing gray scale images of 30 × 30 mm^2 in real-time. The drop tower had an instrumented tup for recording the impact force history and a pair of anvils for recording support reaction histories. The set-up also included a delay/trigger generator to produce a trigger pulse with an appropriate time delay when the tup contacted the specimen. Since all images were recorded during the dynamic event lasting a few hundred microseconds, two high-intensity flash lamps were used to illuminate the specimen surface. Additional experimental details can be found in Refs. [12,13].

The displacement fields in the crack tip vicinity were analyzed using overdeterministic least-squares analysis in conjunction with 2D plane stress expressions

$$u = \sqrt{\frac{r}{2\pi}}\frac{1+\nu}{E}\left[\left(k\cos\frac{\theta}{2} - \frac{1}{2}\cos\frac{3\theta}{2} - \frac{1}{2}\cos\frac{\theta}{2}\right)K_{\mathrm{I}} + \left(k\sin\frac{\theta}{2} + \frac{1}{2}\sin\frac{3\theta}{2} + \frac{3}{2}\sin\frac{\theta}{2}\right)K_{\mathrm{II}}\right] + \cdots$$

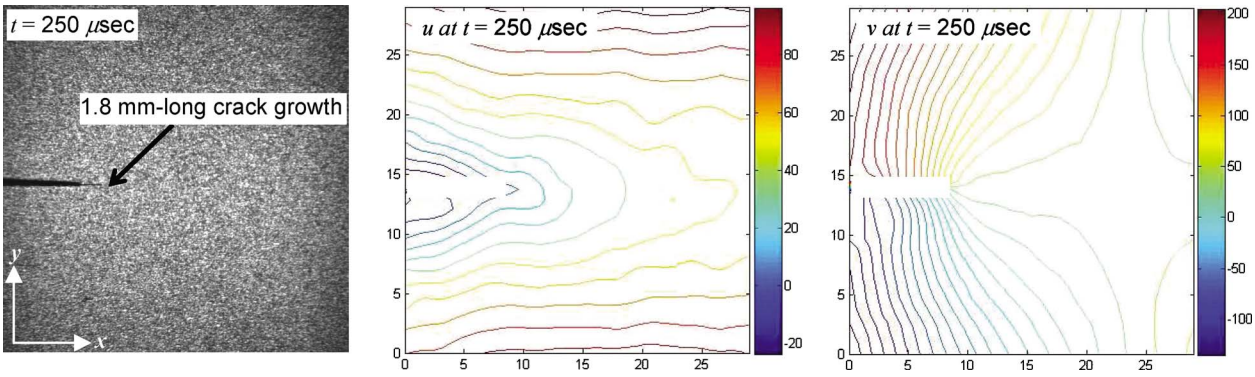

Fig. 4 Sliding (u) and opening (v) displacement fields assessed from image correlation for a dynamic case of neat PETI-5. The image represents the event occurred at t=250 μs (10 μs after crack initiation). Each contour represents a displacement increment of 10 μm and the scale is in mm.

$$v = \sqrt{\frac{r}{2\pi}}\frac{1+\nu}{E}\left[\left(k\sin\frac{\theta}{2} - \frac{1}{2}\sin\frac{3\theta}{2} + \frac{1}{2}\sin\frac{\theta}{2}\right)K_{\mathrm{I}} + \left(-k\cos\frac{\theta}{2} - \frac{1}{2}\cos\frac{3\theta}{2} + \frac{3}{2}\cos\frac{\theta}{2}\right)K_{\mathrm{II}}\right] + \cdots \tag{2}$$

for a dynamically loaded stationary crack and

$$u = \frac{K_{\mathrm{I}}B_{\mathrm{I}}(V)}{\mu}\sqrt{\frac{2}{\pi}}\left(r_1^{1/2}\cos\frac{\theta_1}{2} - r_2^{1/2}\frac{2\alpha_1\alpha_2}{1+\alpha_2^2}\cos\frac{\theta_2}{2}\right) + \frac{K_{\mathrm{II}}B_{\mathrm{II}}(V)}{\mu}\sqrt{\frac{2}{\pi}}\left(r_1^{1/2}\sin\frac{\theta_1}{2} - r_2^{1/2}\frac{1+\alpha_2^2}{2}\sin\frac{\theta_2}{2}\right) + \cdots$$

$$v = \frac{K_{\mathrm{I}}B_{\mathrm{I}}(V)}{\mu}\sqrt{\frac{2}{\pi}}\left(-r_1^{1/2}\alpha_1\sin\frac{\theta_1}{2} + r_2^{1/2}\frac{2\alpha_1}{1+\alpha_2^2}\sin\frac{\theta_2}{2}\right) + \frac{K_{\mathrm{II}}B_{\mathrm{II}}(V)}{\mu}\sqrt{\frac{2}{\pi}}\left(r_1^{1/2}\alpha_1\cos\frac{\theta_1}{2} - r_2^{1/2}\frac{1+\alpha_2^2}{2\alpha_2}\cos\frac{\theta_2}{2}\right) + \cdots \tag{3}$$

for a dynamically propagating crack [16].

In Eq. (2), K_{I} and K_{II} are the stress intensity factor in mode-I and mode-II, respectively. The polar coordinates r and θ indicate the radial and angular distances, respectively, with respect to the crack tip. E, μ, and ν are Young's modulus, shear modulus, and Poisson's ratio, respectively. The symbol k is $(3-\nu)/(1+\nu)$ for plane stress condition. Other parameters appearing in Eq. (3) are defined as follows:

$$r_j = \sqrt{x^2 + \alpha_j^2 y^2}, \quad \theta_j = \tan^{-1}\left(\frac{\alpha_j y}{x}\right) \quad j = 1,2, \quad \alpha_1^2 = 1 - \left(\frac{V}{c_l}\right)^2,$$

$$\alpha_2^2 = 1 - \left(\frac{V}{c_s}\right)^2$$

$$B_{\mathrm{I}}(V) = \frac{1+\alpha_2^2}{4\alpha_1\alpha_2 - (1+\alpha_2^2)^2}, \quad B_{\mathrm{II}}(V) = \frac{2\alpha_2}{4\alpha_1\alpha_2 - (1+\alpha_2^2)^2},$$

$$c_l = \sqrt{\frac{(k+1)\mu}{(k-1)d}}, \quad c_l = \sqrt{\frac{\mu}{d}} \tag{4}$$

in which x and y are crack tip Cartesian coordinates, c_l is the longitudinal wave speed, c_s is the shear wave speed, V is the crack tip velocity, and d is the mass density.

An example of crack opening and sliding displacement contours at two different instants of time after impact are shown in Fig. 4. Each contour represents a displacement increment of 10 μm. Using these measured displacements, the stress intensity factor (SIF) history for PETI-5 samples was determined and two such results are presented in Fig. 5. Evidently, for both samples, the increase in the $K_{\mathrm{I}}(t)$ is linear and monotonic as in the quasi-static case (the zero off-set seen here is attributed to the time delay for stress waves to arrive from the impact point to the crack tip after reflection from the free edge containing the crack). The stress intensity factor at crack initiation ($K_{\mathrm{I}c}$) is 5.1 ± 0.2 MPa(m)$^{1/2}$, ~20% higher than the static value. The crack growth occurred in PETI-5 at speeds ranging between 150 m/s and 250 m/s.

5 Comparison of Neat PETI-5 With Neat 3900

Many fiber reinforced composites use epoxy as the matrix material for benefits over phenolic and polyester families [17]: Epoxy resin adheres very well to a wide variety of reinforcing materials. Under high temperature and pressure, epoxy resin exhibits low viscosity and high wettability so that it flows through the reinforcement phase and fills air pockets. Further, the chemical reaction between epoxy resin and hardener does not release volatiles or moisture, reducing the problem of void formation and disbonding. However, due to its lower glass transition temperature, it has been shown that epoxy resins are less desirable for operation at elevated temperatures [18]. In the current work, a toughened epoxy resin, 3900, popular in the aerospace community, was studied for comparing PETI-5 responses. The in-house measurement of properties for both PETI-5 and 3900 is listed in

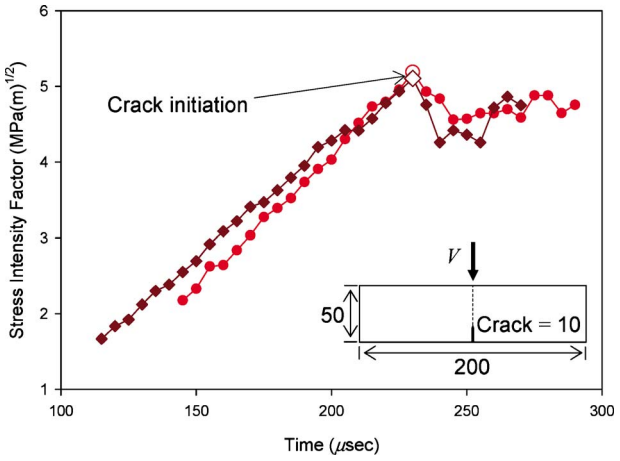

Fig. 5 Dynamic stress intensity factor histories for two neat PETI-5 tests under impact loading. Inset indicates geometry of a specimen used in the test (units in mm). Impact velocity =4.8 m/s and t=0 corresponds to impact.

Table 2 Quasi-static tensile properties of PETI-5 and 3900 at room temperature (measured by strain gauges)

	E (GPa)	ν	σ^u (MPa)	ε^u (%)	d (kg/m^3)
PETI-5	3.25 (±0.20)	0.37 (±0.01)	116.4 (±2.4)	32.8 (±1.2)	1335
3900	2.40 (±0.01)	0.38 (±0.01)	64.4 (±4.3)	3.15 (±0.12)	1234

Table 2. In this comparison, one can readily see that 3900 has lower elastic modulus, although Poisson's ratio is similar. However, the ultimate stress and strain characteristics of PETI-5 are considerably higher than that of the epoxy system (see Fig. 6).

As described in Sec. 3, split-Hopkinson bar test was carried out on four 3900 neat epoxy specimens (the raw data recorded during the SHPB tests for 3900 are shown in the Appendix). The resulting dynamic stress-strain responses for neat 3900 for a strain rate of ~1600 s^{-1} are summarized in Fig. 7. The ultimate strain measured here is 6.5% (±0.6%), whereas the ultimate stress was found at 65.3 (±0.7) MPa. To give clear insight of their tensile behavior under dynamic conditions, averaged stress-strain response for PETI-5 is also provided in Fig. 7. While PETI-5 tends to embrittle at high-strain rates, much higher failure strain and ultimate strength relative to 3900 are evident from the plot.

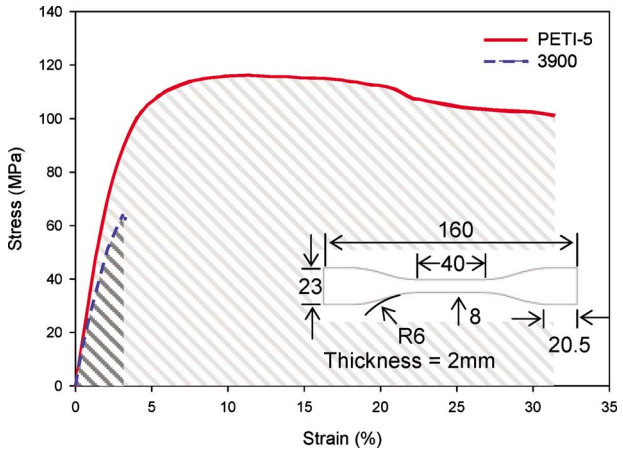

Fig. 6 Comparison of quasi-static (strain rate ~4×10^{-4}/s) stress-strain response of PETI-5 and 3900

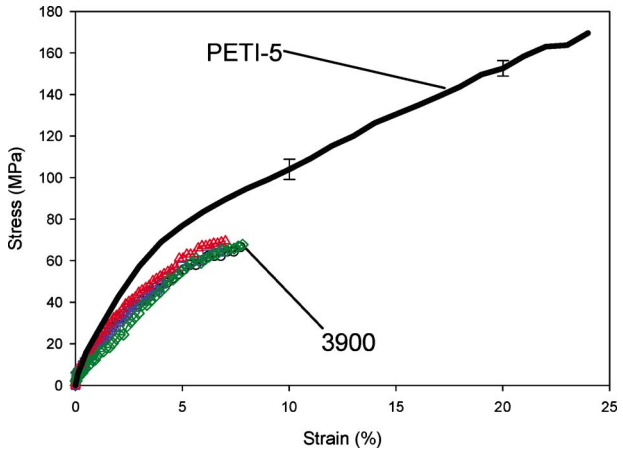

Fig. 7 Tensile stress-strain responses for four Hexcel 3900 dynamic tensile tests carried out using split-Hopkinson bar apparatus (strain rate ~1600/s) in comparison with averaged stress-strain (strain rate ~2000/s) response of PETI-5

The fracture behavior studied here also shows that PETI-5 has substantially higher crack initiation toughness. The SIF histories for both PETI-5 and 3900 are shown in Fig. 8. Each data point in the plot corresponds to an image recorded at an imposed load point displacement. Evidently, up to crack initiation, the stress intensity factor of PETI-5 increases in a monotonic linear fashion, even though it exhibited substantial nonlinearity in stress-strain variation. The crack initiation resulted in an abrupt failure of the specimen. At initiation, the critical stress intensity factor (K_{Ic}) was found to be 4.3 MPa(m)$^{1/2}$. From quasi-static tests for 3900, it was found that the fracture toughness was 1.22 MPa(m)$^{1/2}$, 3–4 times lower than that for PETI-5, as shown in Fig. 8.

Neat PETI-5 and 3900 specimens of identical dimensions (50 $\times$200$\times$9 mm^3) and loading configuration were tested under impact loading (impact velocity at ~4.8 m/s). A comparison of SIF histories for 3900 and PETI-5 samples is presented in Fig. 9(*a*). The major differences are regarding crack initiation time and the corresponding stress intensity factor at initiation. The crack initiation time following impact for 3900 is about 50 μs lower than that for PETI-5. The corresponding stress intensity factor (critical dynamic stress intensity factor or $K_{I\text{-}cr}$) for PETI-5 is ~5.1 MPa(m)$^{1/2}$. The dynamic $K_{I\text{-}cr}$ for 3900 on the other hand is ~2.5 MPa(m)$^{1/2}$, less than half than that for PETI-5. Furthermore, stress intensity factors increase monotonically up to crack initiation. Following initiation, after a noticeable drop in the stress intensity factor value, they continue to remain nearly constant, fluctuating around a steady-state value of approximately 4.5 MPa(m)$^{1/2}$; for 3900, it was 2.5 MPa(m)$^{1/2}$. PETI-5 also shows better crack growth characteristic relative to 3900 and is shown in Fig. 9(*b*). Although crack tip velocities of two materials are nearly the same (the graphs are essentially parallel to each other), higher crack acceleration following crack initiation can be seen in 3900 and thus crack extension is consistently higher throughout the rest of the fracture event.

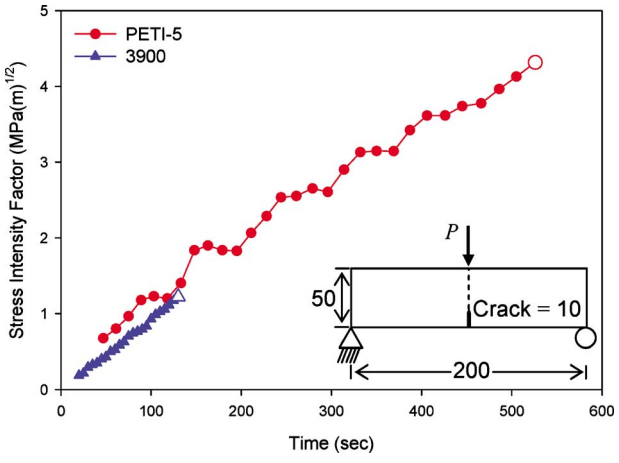

Fig. 8 Comparison of quasi-static stress intensity factors for PETI-5 and 3900 determined from three-point symmetric bend tests at 0.005 mm/s on single edge notch (SEN) samples using DIC. Beam dimensions are in mm and open symbols indicate value at sudden fracture.

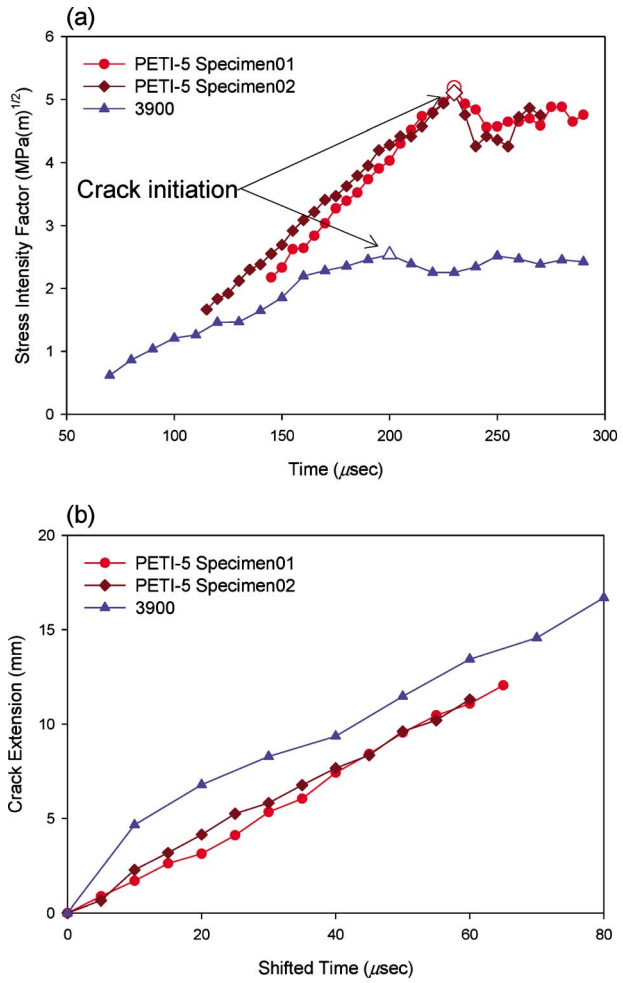

Fig. 9 (*a*) Stress intensity factor history and (*b*) crack extension history of neat PETI-5 and 3900 under dynamic loading (impact velocity 4.8 m/s). Time zero in (*b*) indicates the time when crack initiation takes place.

Fractographic examination was made in order to study characteristics of the two in terms of fracture surface roughness (see Fig. 10). The differences in the fracture surface features between the two are rather striking. PETI-5 surface shows numerous parabolic features with their vertices generally pointing away from the propagating crack front. Such features are common when crack pinning occurs in filled-polymers, with particles acting as physical obstructions to crack propagation, causing significant dissipation of energy. Furthermore, the midplane of the specimen of PETI-5 has relatively fewer of these features when compared with the specimen edges (close to the free surfaces), suggesting a thickness effect commonly seen in ductile metallic materials. No such thickness effect was seen (not shown) readily evident in 3900.

6 Dynamic Fracture Response of IM7/PETI-5 Composites

In this section, dynamic fracture tests were carried out to evaluate fracture parameters of unidirectional IM7/PETI-5 composites with graphite fiber reinforcement. The results are compared with those for T800/3900-2 graphite/epoxy used by NASA. Material properties of IM7/PETI-5 used are listed in Table 3. Also listed are properties of T800/3900-2 unidirectional laminates with which IM7/PETI-5 fracture responses will be compared later on.

As-received test samples, fabricated at NASA Langley, were $50\times200\times5$ mm^3, comprised of 35 plies. The specimens were sprayed with black-and-white paint mists, creating random speckles for implementing 2D DIC technique in conjunction with high-speed digital photography. As in the case of neat PETI-5, the unidirectional IM7/PETI-5 composite coupons were tested under impact loading (impact velocity at ~4.8 m/s). The experimental procedure used was the same as the one described earlier.

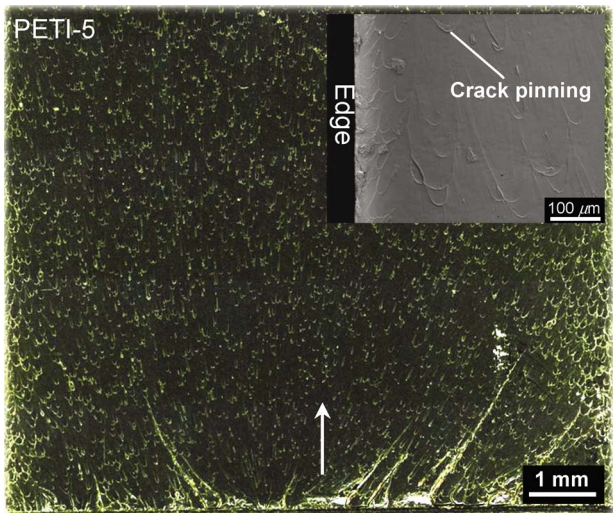

Fig. 10 Fracture surface of PETI-5. Arrow indicates crack growth direction. Numerous parabolic surface features both on the midplane and near free surface in the SEM image are clearly evident.

From the recorded gray scale images of surface speckles, displacement fields in crack growth direction (x-direction in Fig. 11) and sample-length direction (y-direction in Fig. 11) were obtained using 2D DIC, along with crack initiation time, instantaneous crack speed, and stress intensity factor histories. For an illustration, a few selected photographed images with corresponding obtained displacement fields are presented in Fig. 11.

The dynamic crack initiation and growth occurred in the IM7/PETI-5 composite coupons with crack speeds not higher than 300 m/s. Representative crack growth histories are shown in Fig. 12(a). It must be noted that crack extension histories were smoothed by a cubic Bezier curve (smoothing parameter=0.5, chosen because it was desired that a smoothed data point should be located midway from a data point to an adjacent point) before velocities were computed. It is noteworthy that maximum velocity is approximately 300 m/s for IM7/PETI-5 with fiber orientation angle $\beta=0$ deg. This is considerably lower than the ones observed for T800/3900-2 (see Fig. 12(b)) in an earlier investigation [22]. The maximum velocity for 45 deg IM7/PETI-5 is also much lower than that of T800/3900-2, 250 m/s versus 500 m/s.

As described earlier, two sets of 32 speckle images (eight-bit, 1000×1000 pixels) from the undeformed and deformed states were used to perform digital image correlation. The spatial position of a deformed subimage relative to its undeformed counterpart was sought using the image analysis procedure discussed ear-

Table 3 List of elastic constants for IM7/PETI-5 composite laminate

	Ref. [19][a]	Ref. [20]	Ref. [21]	T800/3900-2 [22]
E_1(GPa)	151.7	140–160	175	171.6
E_2(GPa)	9.65	-	-	8.25
G_{12}(GPa)	4.14	-	-	6.21
ν_{12}	0.33	-	-	0.344
σ^u(GPa)	-	0.8–1.3	2.93	-
d(kg/m^3)	1580	-	-	1590

[a]Values used in the current work.

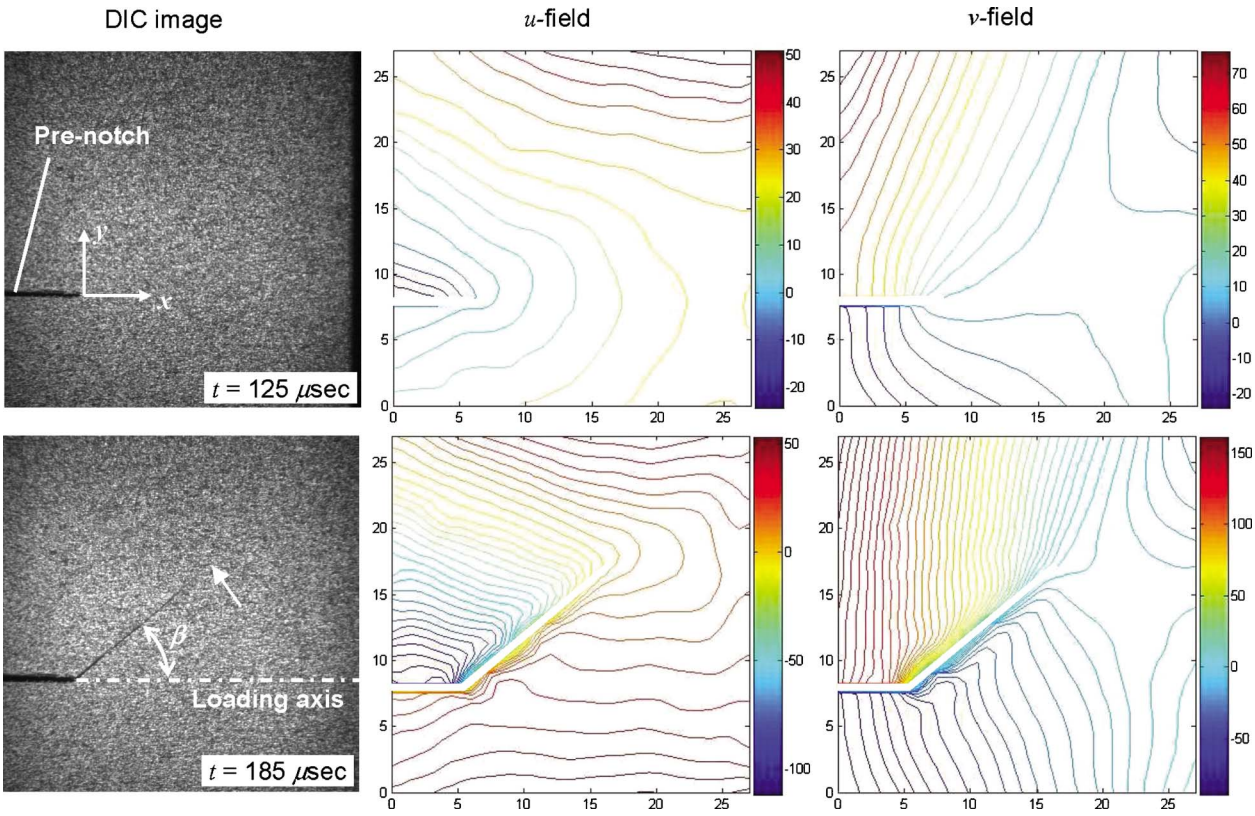

Fig. 11 Representative speckle images for the β=45 deg case with full-field sliding displacement (u) and opening displacement (v) contours (crack initiates at $t\sim125$ μs). Moving crack tip is indicated by an arrow. Units in the axes of displacement fields are in mm. Color-bar indicates displacement in μm. Contour interval is 5 μm.

lier. The resulting 37×37 array of displacement values were used to compute modes-I and -II stress intensity factors by coupling them with 2D displacement field description in the vicinity of a crack tip in an orthotropic medium [23]

$$u = K_{\mathrm{I}}\sqrt{\frac{2r}{\pi}}\,\mathrm{Re}\left[\frac{1}{\mu_2-\mu_1}(p_1\mu_2 z_1 - p_2\mu_1 z_2)\right] + K_{\mathrm{II}}\sqrt{\frac{2r}{\pi}}\,\mathrm{Re}\left[\frac{1}{\mu_2-\mu_1}(p_1 z_1 - p_2 z_2)\right] + \cdots$$

$$v = K_{\mathrm{I}}\sqrt{\frac{2r}{\pi}}\,\mathrm{Re}\left[\frac{1}{\mu_2-\mu_1}(q_1\mu_2 z_1 - q_2\mu_1 z_2)\right] + K_{\mathrm{II}}\sqrt{\frac{2r}{\pi}}\,\mathrm{Re}\left[\frac{1}{\mu_2-\mu_1}(q_1 z_1 - q_2 z_2)\right] + \cdots \quad (5)$$

where quantities p_j, q_j, and z_j $(j=1,2)$ are defined as

$$p_j = \mu_j^2 s_{11} + s_{12} - \mu_j s_{16}$$

$$q_j = \mu_j s_{12} + \frac{s_{22}}{\mu_j} - s_{26}$$

$$z_j = \sqrt{\cos\,\theta + \mu_j \sin\,\theta} \quad (6)$$

and μ_j $(j=1,2)$ are the two roots of the following equation:

$$s_{11}\mu^4 - 2s_{16}\mu^3 + (2s_{12}+s_{66})\mu^2 - 2s_{26}\mu + s_{22} = 0 \quad (7)$$

with positive imaginary part and s_{ij} $(i,j=1,\ldots,6)$ are the elements of compliance matrix.

Equation (5) represents the displacement fields only under quasi-static loading, yet they can be used to extract fracture parameters in situations when the crack tip is stationary but experiences transient stress waves prior to crack initiation by assuming that the functional form of the crack tip field remains unchanged while all the inertial effects enter the equations through the stress intensity factors. In this work, the same equations were also used to obtain stress intensity factors even after crack initiation by taking advantage of the fact that velocity effects of a moving crack tip on displacement fields were minimum when crack velocity was less than $\sim$500 m/s, as shown by Lee et al. [24]. Using K_{I} and K_{II} obtained from Eq. (5), one can readily compute the instantaneous energy release rate [25]

$$G = \frac{\eta}{2c_{66}R(V)}\sqrt{1-\left(\frac{1+\gamma}{\sqrt{\lambda}\,\eta^2\alpha_1+\alpha_2}\right)}(\alpha_1 K_{\mathrm{I}}^2 + \sqrt{\lambda}\,\alpha_2 K_{\mathrm{II}}^2) \quad (8)$$

for a dynamically moving crack (after crack initiation) and

$$G = s_{11}\sqrt{\frac{1+\rho}{2}}\left(\frac{K_{\mathrm{I}}^2}{\lambda^{3/4}} + \frac{K_{\mathrm{II}}^2}{\lambda^{1/4}}\right) \quad (9)$$

for a dynamically loaded stationary crack (prior to crack initiation) in an orthotropic medium. The parameters in Eqs. (8) and (9) are defined as follows [25]:

$$\lambda = \frac{s_{11}}{s_{22}}, \quad \rho = \frac{2s_{12}+s_{66}}{2\sqrt{s_{11}s_{22}}}, \quad \kappa = \frac{3\sqrt{s_{11}s_{22}}+s_{12}}{\sqrt{s_{11}s_{22}}-s_{12}}, \quad c_l = \sqrt{\frac{c_{11}}{d}},$$

$$c_s = \sqrt{\frac{c_{66}}{d}}$$

$$\alpha_1^2 = 1-\left(\frac{V}{c_l}\right)^2, \quad \alpha_2^2 = 1-\left(\frac{V}{c_s}\right)^2,$$

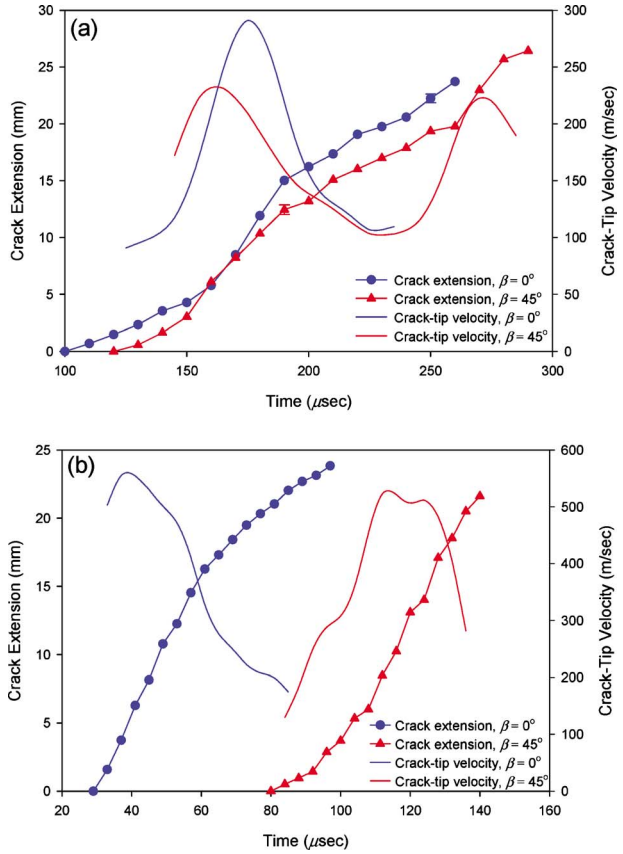

Fig. 12 Crack growth histories and crack tip velocities for (*a*) IM7/PETI-5 and (*b*) T800/3900-2 composites with two different fiber orientations relative to the impact direction. Data for T800/3900-2 are after Ref. [22].

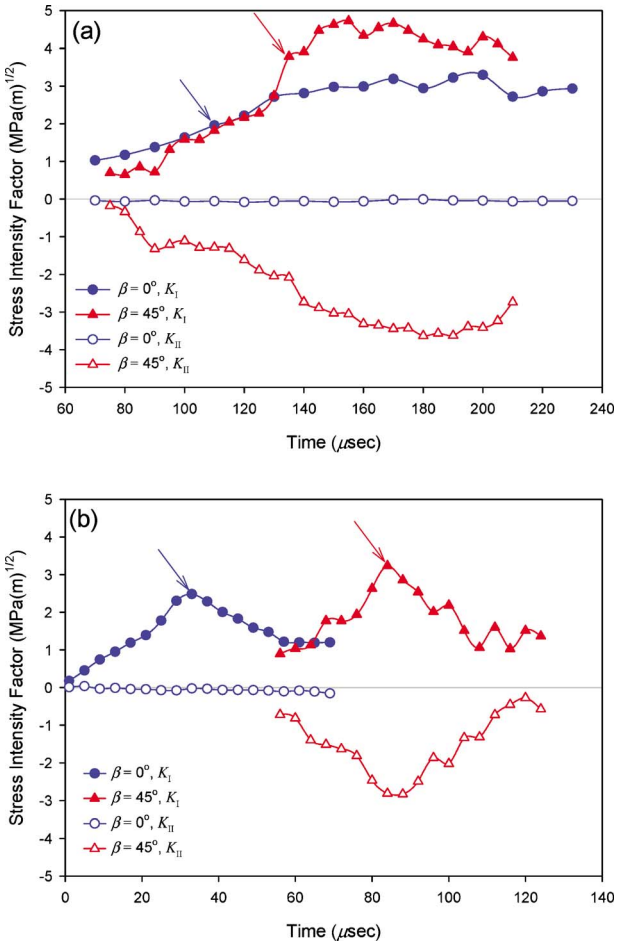

Fig. 13 Modes-I and -II stress intensity factor histories for two fiber orientation angles β=0 deg and 45 deg: (*a*) IM7/PETI-5 and (*b*) T800/3900-2 [25]. Crack initiation values are marked by arrows.

$$\eta^2 = \left(\frac{\kappa+1}{\kappa-1}\right)\left(\frac{3-\kappa+\rho(\kappa+1)}{4\sqrt{\lambda}}\right)$$

$$\gamma = \sqrt{\lambda}\eta^2\frac{3-\kappa}{1+\kappa}, \quad \lambda_j = \frac{\eta^2\alpha_1^2+\mu_j^2}{(1+\gamma)\mu_j} \quad (j=1,2)$$

$$R(V) = \sqrt{\lambda}\eta^2\alpha_1\alpha_2 - \frac{\sqrt{\lambda}\eta^2\alpha_1+\gamma^2\alpha_2}{\sqrt{\lambda}\eta^2\alpha_1+\alpha_2} \tag{10}$$

in which c_{ij} $(i,j=1,\ldots,6)$ are the elements of stiffness matrix for the composite, c_l is the longitudinal wave speed, c_s is the shear wave speed, v is the crack tip velocity, and d is the mass density.

The optically measured modes-I and -II SIF histories for β =0 deg and 45 deg unidirectional panels of IM7/PETI-5 are shown in Fig. 13(*a*), where solid symbols are used for K_{I} and open symbols are used for K_{II}. For comparison, the corresponding modes-I and -II SIF histories for T800/3900-2 graphite/epoxy panels are shown in Fig. 13(*b*) [22]. In Fig. 12(*a*), a monotonic increase in K_{I} values until crack initiation is evident in both cases. As expected, K_{II} values are nearly zero in the former case, whereas it monotonically increases in magnitude in the latter. In the 0 deg case, the SIF values seem to reach an oscillatory but steady value of approximately 2.5 ± 0.2 MPa(m)$^{1/2}$. This value is lower than the one seen for the neat PETI-5 due to crack growth occurring along weak fiber-matrix interfaces. Interestingly, K_{I} values for both angles show a tendency to increase even after crack initiation, unlike the ones for T800/3900-2 graphite/epoxy composites, as seen in Fig. 13(*b*).

With the aid of Eqs. (8) and (9), differences between dynamic fracture toughness of IM7/PETI-5 and T800/3900-2 systems can be demonstrated in Fig. 14. Evidently, crack initiation occurs in IM7/PETI-5 much later than in T800/3900-2 after impact. This is attributed to higher fracture toughness of neat PETI-5 and higher interlaminar fracture toughness of IM7/PETI-5. For β=0 deg, crack initiation time difference is approximately 77 μs, whereas

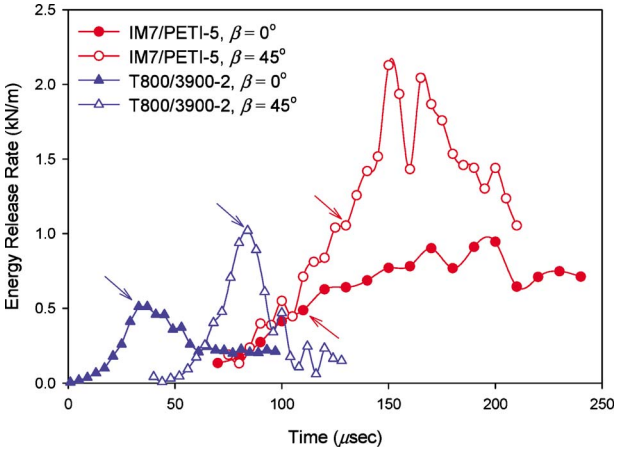

Fig. 14 Energy release rate histories for T800/3900-2 and IM7/PETI-5 composite for 0 deg and 45 deg fiber orientations relative to the impact/initial notch orientation direction (crack initiation is indicated by arrows): delayed crack initiation and higher fracture toughness for IM7/PETI-5 are evident

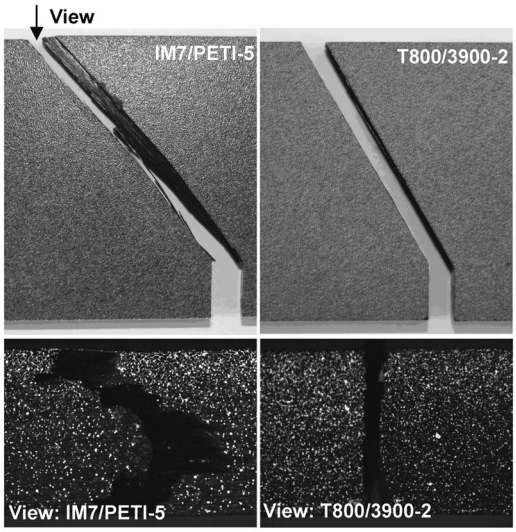

Fig. 15 Fractographic examination of fractured T800/3900-2 and IM7/PETI-5 (β=45 deg) samples: substantially higher roughness due to fiber pull-out is evident in IM7/PETI-5 relative to the one for T800/3900-2

the difference is about 46 μs when β=45 deg. In the former case, characteristics of the matrix dominate the fracture response than in the latter. Another significant difference is the magnitude and variation of energy release rate G. The value of G at crack initiation (G_{in}) for T800/3900-2 and IM7/PETI-5 are both ~0.5 kN/m for 0 deg and ~1.0 kN/m for 45 deg. These suggest that in both these composite systems, dynamic G_{in} values are nearly identical. However, the G histories show different characteristics in the post-initiation regime. T800/3900-2 shows a gradual increase in G up to crack initiation and a continuous drop subsequently for both fiber orientations, resulting in maximum G approximately equal to G_{in}. However, G values for IM7/PETI-5 continues to increase well past crack initiation, attaining a maximum value before a precipitous decrease. Maximum values of G for IM7/PETI-5 are 0.95 kN/m and 2.13 kN/m for 0 deg and 45 deg fiber orientations, respectively, almost 2 times higher than their T800/3900-2 counterparts, suggesting the superiority of IM7/PETI-5 from the perspective of dynamic crack growth resistance.[4]

Post mortem examination of fractured surfaces revealed the IM7/PETI-5 composites to have significantly irregular surfaces features, whereas T800/3900-2 showed relatively flat surfaces with a near-glossy appearance. Photographs of the two halves of the fractured specimens for β=45 deg are shown in Fig. 15. Fracture surfaces of T800/3900-2 appear nearly perpendicular to the specimen surfaces and very few undulations from view (from the top of the specimen). To the contrary, the fracture surfaces of IM7/PETI-5 are neither perpendicular to the specimen surfaces nor flat at the same optical magnification. Quantification of roughness by fractal dimension is a common practice [26] but a simpler measure, the profile roughness parameter (R_L), is employed here for brevity. It is defined as the ratio of the total profile length to the projected length of the profile [27]. The estimated value of R_L for T800/3900-2 is ~1.1, whereas that of IM7/PETI-5 is ~2.8 when the sectioning plane is placed on the outermost edge. That is, fracture surface roughness of T800/3900-2 is very close to that of a flat surface (R_L=1), whereas that of IM7/PETI-5 is nearly 3 times that of T800/3900-2. Smoothness and roughness of the two materials are clearly contrasted in the fracture surface (not shown). The surface of T800/3900-2 shows a relatively smooth appearance, whereas its IM7/PETI-5 counterpart shows a measurably rough appearance with significant amount of visible bare fiber bundles. Such protruded fibers or fiber bundles are due to fiber pull-out, which is one of the failure mechanisms in tough fiber reinforced composites [28].

[4]This observation also emphasizes the need for using full-field real-time deformation measurements in favor of conventional global measurements, such as crack initiation load, to assess critical fracture parameters. That is, if crack initiation toughness alone was evaluated for these two composites, say, using global crack initiation load measurement, one might come to the conclusion that the two material systems have similar fracture performance. This, however, is incorrect if post-initiation responses of the two materials, measured optically in this case, are taken into consideration, showing the superiority of PETI-5 based composite.

7 Conclusions

Tensile and fracture properties of neat PETI-5 and IM7/PETI-5 composites were evaluated under quasi-static and elevated rates of loading. The results were compared with those obtained for 3900 and T800/3900-2, respectively. Besides conventional mechanical testing, high-strain rate tensile tests and dynamic fracture tests were carried out on neat and composite specimens. A 2D digital image correlation method and high-speed photography were employed to evaluate dynamic fracture parameter histories. The following are some of the major observations of this study.

- PETI-5 shows strain rate sensitivity. At two different strain rates, the three material properties evaluated, namely, stress at failure, stress intensity factor at crack initiation, and strain at failure, all show measurable differences. The former two increased with increasing loading rate by approximately 50% and 20%, respectively, but the latter decreased by about 25%.
- Relative to 3900, under the quasi-static loading conditions, neat PETI-5 exhibited excellent tensile strength (2 times higher), failure strain (10 times higher), strain energy density (30 times higher), crack initiation toughness (4 times higher), delayed crack initiation, and lower crack speed. This superiority of PETI-5 prevails for both quasi-static and dynamic loading conditions. Under dynamic loading conditions (strain rate of 1600–2000 s^{-1}), neat PETI-5 exhibited 3 times higher in tensile strength, 4 times higher in failure strain, and 2 times higher in crack initiation toughness relative to neat 3900.
- Fracture surface of PETI-5 showed surface texture variation in the thickness direction with more numerous features close to the surface than the interior. The crack front pinning and chain extension features dominate the fracture surface when compared with cleavage fracture of 3900.
- Regardless of the fiber orientation, IM7/PETI-5 composites exhibited higher SIFs, higher energy release rate, delayed crack initiation time, and lower crack speed during dynamic growth relative to T800/3900-2. However, at crack initiation, both SIF and energy release rates were found to be nearly the same. Interestingly, however, the energy release rate in IM7/PETI-5 composites increased, following crack initiation, by nearly a factor of 2, before showing a decreasing trend. This is unlike T800/3900-2 fracture response, where energy release rates dropped precipitously, following crack initiation, suggesting a superior crack growth resistance in the former.
- Fracture surfaces of T800/3900-2 were nearly featureless. On the contrary, IM7/PETI-5 surfaces show high roughness, crack front tortuosity, fiber bridges consistent with the observed fracture parameters.

Acknowledgment

This research was sponsored by NASA Langley Research Center under a Grant/Cooperative Agreement (Grant No. NNX07AC64A) with Auburn University, AL. We would also like to acknowledge the assistance of Mr. Mark Scott from Hexcel, Inc. for providing the 3900 neat resin plaques.

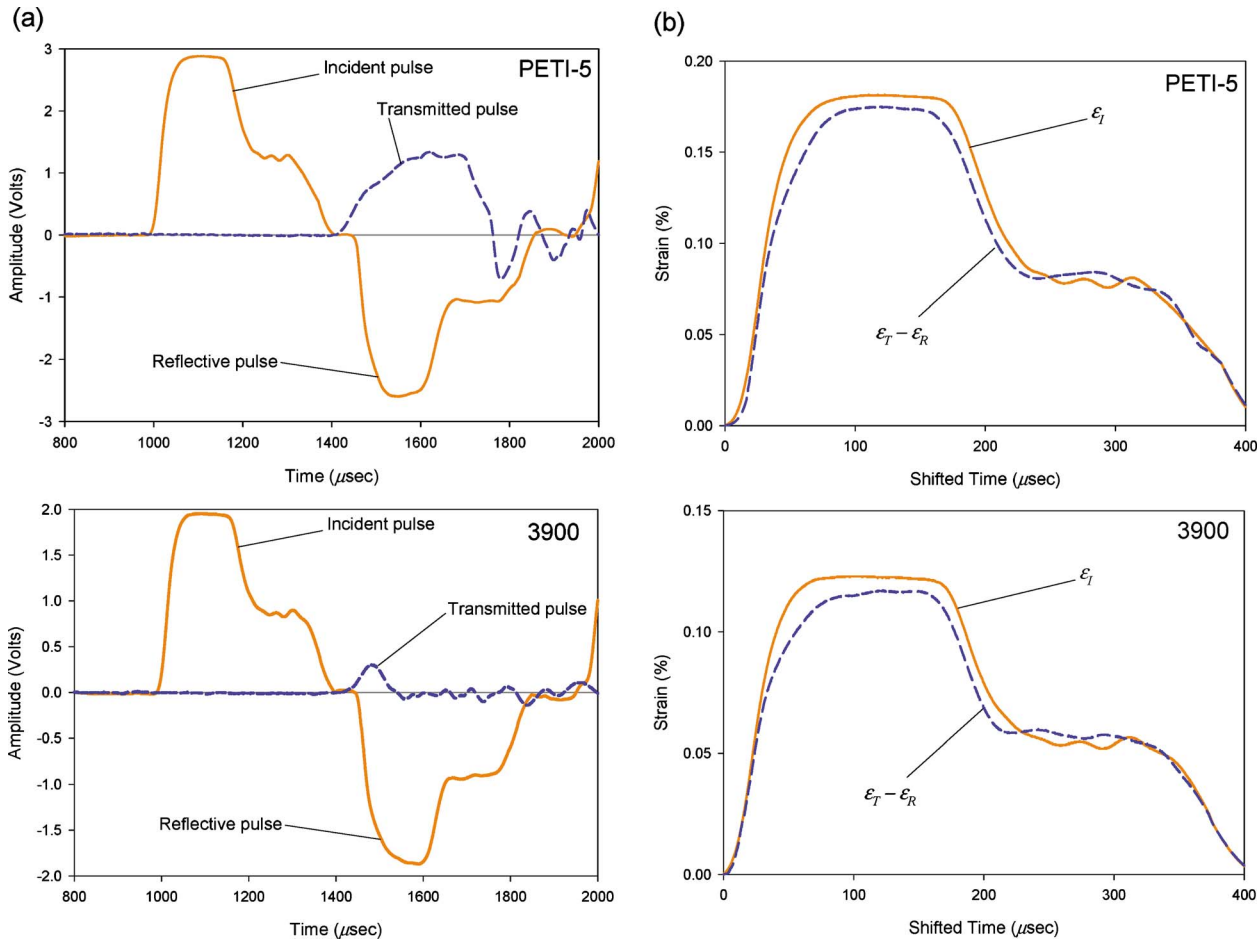

Fig. 16 Strain signals for PETI-5 and 3900 from tensile split-Hopkinson bar apparatus. (*a*) Typical incident, reflected, and transmitted waveforms and (*b*) overlay of ε_I and $\varepsilon_T - \varepsilon_R$ signals on a shifted time axis.

Appendix

The raw signals measured in the tensile split-Hopkinson bar apparatus used for dynamic tensile tests are reported here. For PETI-5, the strain gauge used on the incident bar is CEA-13-125UW-120 with a gauge factor (GF) of 2.12. The gauge used on the transmitter bar is CEA-13-062UW-120 (GF=2.13). While testing 3900, however, this set-up was slightly modified by using a strain gauge with a higher gauge factor in order to amplify the weak transmitted strain signal. The gauge used on the transmitter bar was replaced with WD-DY-062AP-350 (GF=3.26) for testing 3900. All strain gauges were acquired from Vishay Micro-Measurements, Inc., Raleigh, NC.

In both cases, strain at failure and stress at failure were attained within the duration of the pulse generated by impacting striker. In the PETI-5 case, stress reaches the maximum at ~150 μs, about 20 μs shorter than the loading pulse duration (see Fig. 16(*a*)). Similarly, for 3900, pulse duration is approximately 165 μs, whereas maximum stress occurs at ~70 μs. Furthermore, the specimens are in reasonably good dynamic equilibrium, as evident in Fig. 16(*b*).

References

[1] Fenbert, J. W., Ozoroski, L. P., Geiselhart, K. A., Shields, E. W., and McElroy, M. O., 1999, "Concept Development of a Mach 2.4 High-Speed Civil Transport," Report No. NASA/TP-1999-209694.

[2] Hou, T. H., Jensen, B. J., and Hergenrother, P. M., 1996, "Processing and Properties of IM7/PETI Composites," J. Compos. Mater., **30**(1), pp. 109–122.

[3] Plunkett, R. B., Tsang, P. H., Lesko, J. J., Wood, J. D., and Rufin, A. C., 1996, "Assessment of Residual Composite Properties as Influenced by Thermal Mechanical Aging," ASME Aerospace Division (Publication) Vol. AD, 52, pp. 405–411.

[4] Cano, R. J., and Jensen, B. J., 1997, "Effect of Molecular Weight on Processing and Adhesive Properties of the Phenylethynyl-Terminated Polyimide LARC™-PETI-5," J. Adhes., **60**(1–4), pp. 113–123.

[5] Johnson, T. F., and Gates, T. S., 2001, "High Temperature Polyimide Materials in Extreme Temperature Environments," AIAA 2001-1214, AIAA/ASME/ASCE/AHS/ASC Structures, Structural Dynamics and Materials Conference, Vol. 1, pp. 273–284.

[6] Whitley, K. S., and Gates, T. S., 2002, "Thermal/Mechanical Response and Damage Growth in Polymeric Composites at Cryogenic Temperatures," AIAA 2002-1416, AIAA/ASME/ASCE/AHS/ASC Structures, Structural Dynamics and Materials Conference, Vol. 3, pp. 1677–1689.

[7] Han, M.-H., and Nairn, J. A., 2003, "Hygrothermal Aging of Polyimide Matrix Composite Laminates," Composites, Part A, **34**(10), pp. 979–986.

[8] Jensen, B. J., Bryant, R. G., and Wilkinson, S. P., 1994, "Development of a Unique Copolyimide Backbone for High Temperature Adhesives With Thermal Reactive Groups," Polym. Prepr. (Am. Chem. Soc. Div. Polym. Chem.), **35**(1), pp. 539–540.

[9] Smith, J. G., Jr., and Hergenrother, P. M., 1994, "Chemistry and Properties of Phenylethynyl Phthalic Anhydride Imide Oligomers," Polym. Prepr. (Am. Chem. Soc. Div. Polym. Chem.), **35**(1), pp. 353–354.

[10] Marur, P., and Tippur, H. V., 1998, "Evaluation of Mechanical Properties of Functionally Graded Materials," J. Test. Eval., **26**(6), pp. 539–545.

[11] Owens, A. T., and Tippur, H. V., 2008, "Tensile Stress-Strain Response of Glass-Filled Epoxy Under Elevated Rates of Loading Using a Split Hopkinson Bar Apparatus," Exp. Mech., **49**(6), pp. 799–811.

[12] Kirugulige, M. S., Tippur, H. V., and Denney, T. S., 2007, "Measurement of Transient Deformations Using Digital Image Correlation Method and High-Speed Photography: Application to Dynamic Fracture," Appl. Opt., **46**(22), pp. 5083–5096.

[13] Kirugulige, M. S., and Tippur, H. V., 2009, "Measurement of Fracture Parameters for a Mixed-Mode Crack Driven by Stress Waves Using Image Correlation Technique and High-Speed Digital Photography," Strain, **45**(2), pp. 108–122.

[14] Morozov, V. A., 1993, *Regularization Methods for Ill-Posed Problems*, CRC, Ann Arbor, MI.

[15] Reinsch, C. H., 1967, "Smoothing by Spline Functions," Numerische Math-

ematik, **10**, pp. 177–183.
[16] Nishioka, T., and Atluri, S. N., 1983, "Path Independent Integrals, Energy Release Rates, and General Solutions of Near-Tip Fields in Mixed-Mode Dynamic Fracture Mechanics," Eng. Fract. Mech., **18**(1), pp. 1–22.
[17] Penn, L. S., and Chiao, T. T., 1982, "Epoxy Resins," *Handbook of Composites*, G. Lubin, ed., Reinhold, New York, pp. 57–88.
[18] Ku, H., Cardona, F., Rogers, D., and Vandenbroucke, A., 2008, "Effects of EPON on Mechanical and Thermal Properties of Epoxy Resins," Adv. Mater. Res., **47–50**, pp. 536–539.
[19] Ural, A., Zehnder, A., and Ingraffea, A., 2003, "Fracture Mechanics Approach to Facesheet Delamination in Honeycomb: Measurement of Energy Release Rate of the Adhesive Bond," Eng. Fract. Mech., **70**(1), pp. 93–103.
[20] Veazie, D. R., Siochi, E. J., and Lindsay, J. S., 2001, "Effects of Resin Consolidation on the Durability of IM7/PETI-5 Composites," Journal of Composites Technology and Research, **23**(1), pp. 28–35.
[21] Hou, T. H., Cano, R. J., and Jensen, B. J., 1998, "IM7/LARC™ MPEI-1 Polyimide Composites," High Perform. Polym., **10**(2), pp. 181–192.
[22] Lee, D., Tippur, H., Kirugulige, M., and Bogert, P., 2009, "Experimental Study of Dynamic Crack Growth in Unidirectional Graphite/Epoxy Composites Using Digital Image Correlation and High-Speed Photography," J. Compos. Mater., **43**(19), pp. 2081–2108.
[23] Sih, G. C., Paris, P. C., and Irwin, G. R., 1965, "On Cracks in Rectilinearly Anisotropic Bodies," Int. J. Fract. Mech., **1**(3), pp. 189–203.
[24] Lee, D., Tippur, H. V., and Bogert, P., 2010, "Quasi-Static and Dynamic Fracture of Graphite/Epoxy Composites: An Optical Study of Loading Rate Effects," Composites, Part B, **41**, pp. 462–474.
[25] Liu, C., Rosakis, A. J., and Stout, M. G., 2001, "Dynamic Fracture Toughness of a Unidirectional Graphite/Epoxy Composite," American Society of Mechanical Engineers, Applied Mechanics Division, AMD (ASME-IMECE 2001), Dynamic Failure in Composite Materials and Structures, Vol. 247, pp. 1–12.
[26] Davidson, D. L., 1989, "Fracture Surface Roughness as a Gauge of Fracture Toughness: Aluminium-Particulate SiC Composites," J. Mater. Sci., **24**(2), pp. 681–687.
[27] El-Soudani, S. M., 1978, "Profilometric Analysis of Fractures," Metallography, **11**(3), pp. 247–336.
[28] Cantwell, W. J., and Morton, J., 1991, "The Impact Resistance of Composite Materials—A Review," Composites, **22**(5), pp. 347–362.